PHYSICAL REVIEW B **85**, 165454 (2012)

Orbital magnetic susceptibility of finite-sized graphene

Yuya Ominato and Mikito Koshino
Department of Physics, Tohoku University, Sendai 980-8578, Japan
(Received 31 January 2012; published 30 April 2012)

We study the orbital magnetism of graphene ribbon in the effective-mass approximation, to figure out the finite-size effect on the singular susceptibility known in the bulk limit. We find that the susceptibility at $T = 0$ oscillates between diamagnetism and paramagnetism as a function of ε_F, in accordance with the subband structure formed by quantum confinement. In increasing T, the oscillation rapidly disappears once the thermal broadening energy exceeds the subband spacing, and the susceptibility $\chi(\varepsilon_F)$ approaches the bulk limit, i.e., a thermally broadened diamagnetic peak centered at $\varepsilon_F = 0$. The electric current supporting the diamagnetism is found to flow near the edge with a depth $\sim \hbar v/(2\pi k_B T)$, with v being the band velocity, while at $T = 0$ the current distribution spreads entirely in the sample reflecting the absence of the characteristic wavelength in graphene. The result is applied to estimate the three-dimensional random-stacked multilayer graphene, where we show that the external magnetic field is significantly screened inside the sample in low temperatures, in a much stronger manner than in graphite.

DOI: 10.1103/PhysRevB.85.165454 PACS number(s): 81.05.ue, 75.20.−g, 75.70.Ak

I. INTRODUCTION

Graphite is known as one of the strongest diamagnetic materials among natural substances.[1–3] This property is due to the large orbital diamagnetism related to the small effective mass in the band structure, i.e., narrow energy gap between conduction and valence bands. The diamagnetic effect becomes even greater in graphene monolayer[4–6] which is truly a zero-gap system.[1,7–9] The magnetic susceptibility of graphene at zero temperature contains a singularity expressed as a δ function in Fermi energy ε_F, which diverges at Dirac point ($\varepsilon_F = 0$) where the two bands stick, and vanishes otherwise.[1,10–17] The orbital diamagnetism has been studied for other graphene-related materials, such as graphite intercalation compounds,[18–21] carbon nanotube,[22–24] few-layer graphenes,[25–27] and an organic material having a similar gapless spectrum.[28]

In this paper, we investigate the orbital diamagnetism of a graphene strip with finite width.[29–41] The purpose of this work is twofold: (i) To understand how the δ function singularity of the bulk limit is relaxed in a realistic finite-sized graphene system. In the literature, the orbital susceptibility of graphene nanoribbons was calculated for the Fermi energies near the Dirac point,[31,42] while the behavior off Dirac point and the relation to the bulk susceptibility is not well understood. (ii) To study the diamagnetic current flow on graphene. In the conventional diamagnetism of metal, we usually expect that the current circulates near the surface with a depth of the order of the Fermi wavelength λ_F. In graphene, the only characteristic length scale λ_F intrinsically diverges, and we expect a peculiar current distribution different from the conventional system.

To address above problems, here we calculate the orbital susceptibility and the current distribution of graphene ribbon with an arbitrary width, in various Fermi energies ε_F and temperatures T, using the effective-mass approximation. We find that the susceptibility at $T = 0$ oscillates between diamagnetic and paramagnetic values in increasing ε_F, in accordance with the detailed subband structure. In increasing temperature, the oscillation rapidly disappears once the thermal broadening energy exceeds the subband spacing, and the susceptibility approaches bulk limit, i.e., a thermally broadened diamagnetic peak centered at $\varepsilon_F = 0$, independently of the atomic configuration at the edge. We also apply a similar analysis to the carbon nanotube, and find a similar oscillation in the susceptibility.

The electric current supporting the diamagnetism spreads entirely in the sample at $T = 0$, reflecting the absence of the characteristic wavelength. In increasing temperature, however, the current density tends to localize near the boundary with a depth $\sim\hbar v/(2\pi k_B T)$, forming an edge current circulation.

The analysis of the spatial distribution of the diamagnetic current is useful in studying a graphene stack where the diamagnetic current of one layer influences the electron motion in other layers. If we take a randomly stacked graphene multilayer, in which the interlayer coupling is expected to be small,[43–49] the self-consistent calculation shows that the diamagnetism is much stronger than in graphite, and the external magnetic field is significantly screened inside the sample in low temperatures.

The paper is organized as follows. In Sec. II, we briefly review effective-mass description of electrons in graphene ribbon, and formulate the orbital magnetic susceptibility. We present the numerical results and detailed discussion in Sec. III, as well as a similar analysis for the carbon nanotube in Sec. IV. We argue the diamagnetism of randomly stacked graphene multilayers in Sec. V. The conclusion is given in Sec. VI.

II. FORMULATIONS

A. Effective-mass approximation

Graphene is composed of a honeycomb network of carbon atoms, where a unit cell contains a pair of sublattices, denoted by A and B. Figures 1(a) and 1(b) show the atomic structure of zigzag and armchair graphene ribbons, respectively, where $\boldsymbol{a}$ and $\boldsymbol{b}$ are primitive translation vectors of infinite graphene. The lattice constant is given by $a = |\boldsymbol{a}| \approx 0.246$ nm. For both cases we set the y-axis along the ribbon, and set $x = 0$ and L_x to the line of missing sites nearest from the edge. We define η as the angle between the x axis and $\boldsymbol{a}$, which is $\pi/6$ for the zigzag and 0 for the armchair boundary.

(a) Zigzag ribbon

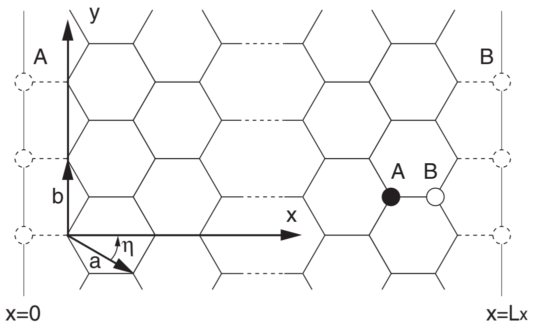

(b) Armchair ribbon

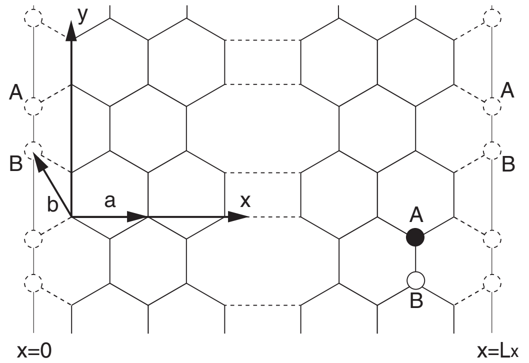

FIG. 1. Atomic structures of graphene ribbons with (a) zigzag boundary and (b) armchair boundary, respectively. Dashed circles indicate missing sites beyond the boundary.

In a tight-binding model, the wave function of the graphene electron is written as

$$\psi(\boldsymbol{r}) = \sum_{\boldsymbol{R}_\mathrm{A}} \psi_\mathrm{A}(\boldsymbol{R}_\mathrm{A})\phi(\boldsymbol{r} - \boldsymbol{R}_\mathrm{A}) + \sum_{\boldsymbol{R}_\mathrm{B}} \psi_\mathrm{B}(\boldsymbol{R}_\mathrm{B})\phi(\boldsymbol{r} - \boldsymbol{R}_\mathrm{B}), \tag{1}$$

where $\boldsymbol{R}_\mathrm{A}$ and $\boldsymbol{R}_\mathrm{B}$ are the positions of A sites and B sites, respectively, and $\phi(\boldsymbol{r})$ denotes the wave function of the p_z orbital of a carbon atom.

For states in the vicinity of the Fermi level $\varepsilon = 0$, the wave amplitudes are written as[50]

$$\begin{aligned} \psi_\mathrm{A}(\boldsymbol{R}_\mathrm{A}) &= e^{i\boldsymbol{K}\cdot\boldsymbol{R}_\mathrm{A}} F_\mathrm{A}^\mathrm{K}(\boldsymbol{R}_\mathrm{A}) + e^{i\eta} e^{i\boldsymbol{K}'\cdot\boldsymbol{R}_\mathrm{A}} F_\mathrm{A}^{\mathrm{K}'}(\boldsymbol{R}_\mathrm{A}),\\ \psi_\mathrm{B}(\boldsymbol{R}_\mathrm{B}) &= -\omega e^{i\eta} e^{i\boldsymbol{K}\cdot\boldsymbol{R}_\mathrm{B}} F_\mathrm{B}^\mathrm{K}(\boldsymbol{R}_\mathrm{B}) + e^{i\boldsymbol{K}'\cdot\boldsymbol{R}_\mathrm{B}} F_\mathrm{B}^{\mathrm{K}'}(\boldsymbol{R}_\mathrm{B}), \end{aligned} \tag{2}$$

in terms of the slowly varying envelope functions $F_\mathrm{A}^\mathrm{K}, F_\mathrm{B}^\mathrm{K}, F_\mathrm{A}^{\mathrm{K}'}$, and $F_\mathrm{B}^{\mathrm{K}'}$. The envelope functions satisfy the Schrödinger equation,[1,7–9,50,51]

$$\mathcal{H}_0 \boldsymbol{F}(\boldsymbol{r}) = \varepsilon \boldsymbol{F}(\boldsymbol{r}), \tag{3}$$

with

$$\mathcal{H}_0 = \hbar v \begin{pmatrix} 0 & \hat{k}_x - i\hat{k}_y & 0 & 0 \\ \hat{k}_x + i\hat{k}_y & 0 & 0 & 0 \\ 0 & 0 & 0 & \hat{k}_x + i\hat{k}_y \\ 0 & 0 & \hat{k}_x - i\hat{k}_y & 0 \end{pmatrix}, \tag{4}$$

$$\boldsymbol{F}(\boldsymbol{r}) = \begin{pmatrix} F_\mathrm{A}^\mathrm{K}(\boldsymbol{r}) \\ F_\mathrm{B}^\mathrm{K}(\boldsymbol{r}) \\ F_\mathrm{A}^{\mathrm{K}'}(\boldsymbol{r}) \\ F_\mathrm{B}^{\mathrm{K}'}(\boldsymbol{r}) \end{pmatrix}, \tag{5}$$

where $\hat{\boldsymbol{k}} = -i\nabla$ and v is the band velocity.

The electronic states of the graphene ribbon can be correctly described by setting the appropriate boundary condition to the effective-mass Hamiltonian.[34] Now the eigenstates are labeled by k_y since the system is translationally symmetric along y. A wave function of k_y and the energy ε is generally written as

$$\boldsymbol{F}(\boldsymbol{r}) = e^{ik_y y} \begin{pmatrix} Ae^{ik_x x} + Be^{-ik_x x} \\ s(Ae^{i(k_x x+\theta)} - Be^{-i(k_x x+\theta)}) \\ Ce^{ik_x x} + De^{-ik_x x} \\ s(Ce^{i(k_x x-\theta)} - De^{-i(k_x x-\theta)}) \end{pmatrix}, \tag{6}$$

where $k_x^2 = \varepsilon^2/\hbar^2 v^2 - k_y^2, e^{i\theta} = (k_x + ik_y)/\sqrt{k_x^2 + k_y^2}$, $s = \varepsilon/|\varepsilon|$, and A, B, C, and D are numbers to be determined by satisfying the boundary condition, as we will argue in the following.

B. Zigzag boundary

In the zigzag ribbon, the boundary condition is given by $\psi_\mathrm{A}(\boldsymbol{R}_\mathrm{A}) = 0$ at $x = 0$, and $\psi_\mathrm{B}(\boldsymbol{R}_\mathrm{B}) = 0$ at $x = L_x$. By using Eq. (2), this is translated to the condition for the envelope function as

$$\begin{aligned} F_\mathrm{A}^\mathrm{K}(0,y) &= 0, \quad F_\mathrm{B}^\mathrm{K}(L_x,y) = 0,\\ F_\mathrm{A}^{\mathrm{K}'}(0,y) &= 0, \quad F_\mathrm{B}^{\mathrm{K}'}(L_x,y) = 0, \end{aligned} \tag{7}$$

which keeps the states at K and those at K′ independent. For an eigenstate for the K point, we apply the first two lines of Eqs. (7) to (6) to obtain

$$A + B = 0, \quad s(Ae^{i(k_x L_x+\theta)} - Be^{-i(k_x L_x+\theta)}) = 0. \tag{8}$$

To have a solution other than $A = B = 0$, we require[34]

$$k_y = \frac{k_x}{\tan k_x L_x}. \tag{9}$$

For given k_y, we define $k_n (n = 0,1,2,\ldots)$ as solution of Eq. (9) in k_x satisfying $n\pi < k_n L_x < (n+1)\pi$. Corresponding eigenstates and the energy are obtained as

$$\boldsymbol{F}_{snk_y}(\boldsymbol{r}) = A_n \frac{e^{ik_y y}}{\sqrt{L_x L_y}} \begin{pmatrix} i\sin k_n x \\ s(-1)^{n+1}\sin k_n(x - L_x) \\ 0 \\ 0 \end{pmatrix},$$

$$A_n = \left(1 - \frac{\sin 2k_n L_x}{2k_n L_x}\right)^{-1/2}, \quad \varepsilon_{snk_y} = s\hbar v\sqrt{k_n^2 + k_y^2}, \tag{10}$$

for $n = 0,1,2,\ldots$. For the normalization of the wave function, we assumed the periodic boundary condition in the y direction with a large enough period L_y.

Solution k_n is obtained by searching for crossing points of $\tan k_x L_x$ and k_x/k_y as illustrated in Fig. 2. When $k_y L_x > 1$,

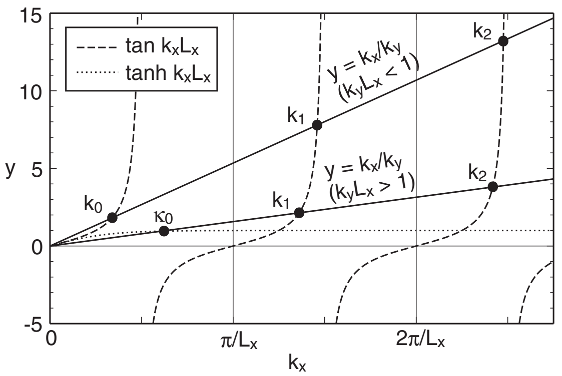

FIG. 2. Plots to find solutions of Eqs. (9) and (11).

the first solution k_0 becomes a pure imaginary number $i\kappa_0$ which satisfies

$$k_y = \frac{\kappa_0}{\tanh \kappa_0 L_x}. \tag{11}$$

The wave function and the energy then becomes

$$\boldsymbol{F}_{s0k_y}(\boldsymbol{r}) = A_0 \frac{e^{ik_y y}}{\sqrt{L_x L_y}} \begin{pmatrix} i \sinh \kappa_0 x \\ -s \sinh \kappa_0 (x - L_x) \\ 0 \\ 0 \end{pmatrix},$$
$$A_0 = \left(-1 + \frac{\sinh 2\kappa_0 L_x}{2\kappa_0 L_x} \right)^{-1/2}, \tag{12}$$
$$\varepsilon_{s0k_y} = s\hbar v \sqrt{-\kappa_0^2 + k_y^2}.$$

This actually describes the edge state localized at the boundary $x = 0$ and L_x giving a nearly flat energy band.[29–31]

The eigenenergy ε_{snk_y} represents the nth branch of conduction ($s = +$) and valence ($s = -$) bands, respectively. The energy-band structure of K as a function of k_y is shown as solid curves in Fig. 3(a). Eigenstates for K′ point are obtained similarly, where the energy-band structure is equivalent to Fig. 3(a) with k_y inverted to $-k_y$. The flat band of edge states of K and K′ are connected in a wave number away from K or K′.[29–31]

C. Armchair boundary

In the armchair ribbon, the boundary condition imposes both of $\psi_A(\boldsymbol{R}_A) = 0$ and $\psi_B(\boldsymbol{R}_B) = 0$ at each of $x = 0$ and $x = L_x$. The corresponding conditions for the envelope functions are written as

$$\begin{aligned} F_A^K(0,y) + F_A^{K'}(0,y) &= 0, \\ F_B^K(0,y) - F_B^{K'}(0,y) &= 0, \\ F_A^K(L_x,y) + \omega^{-2N} F_A^{K'}(L_x,y) &= 0, \\ F_B^K(L_x,y) - \omega^{-2N} F_B^{K'}(L_x,y) &= 0, \end{aligned} \tag{13}$$

where $N = L_x/a$ is the number of honeycomb lattices between $x = 0$ and L_x, which can be an integer or a half integer depending on the position of the edge.

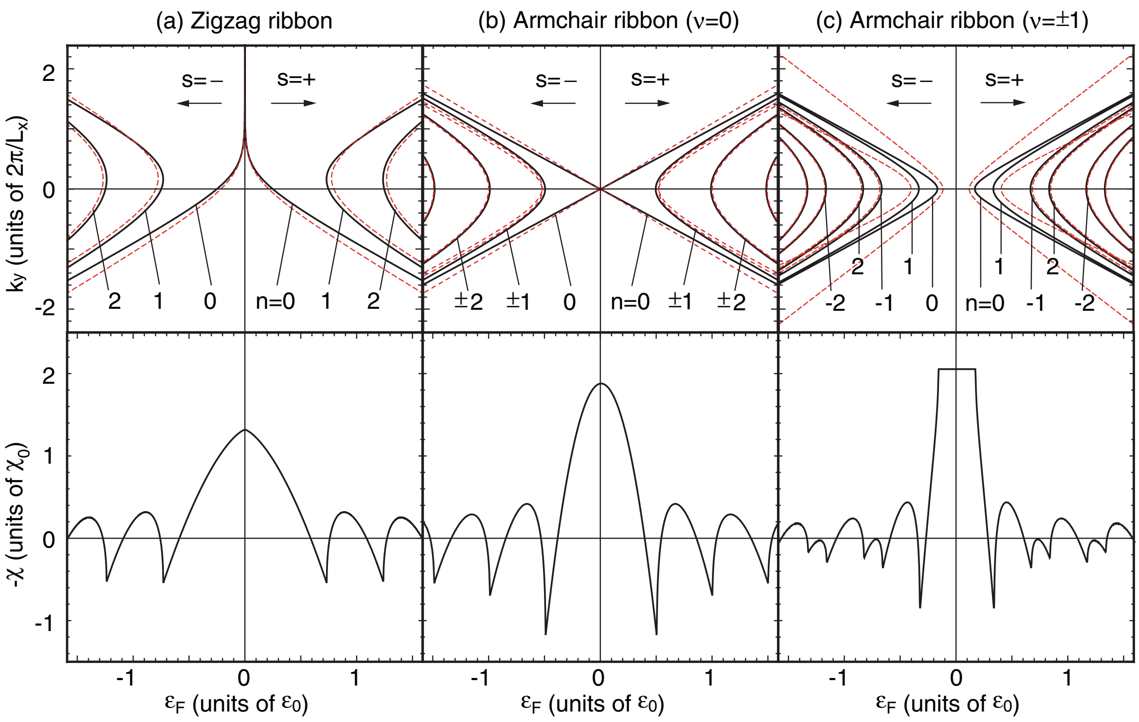

FIG. 3. (Color online) Band structure (upper panel) and magnetic susceptibility as a function of ε_F (lower), of (a) zigzag, (b) metallic armchair ($\nu = 0$), and (c) semiconducting armchair ($\nu = \pm 1$) graphene ribbons. In upper panels, solid (black) and dashed (red) curves indicate the band structures at zero and a finite magnetic field, respectively. For the latter, the energy band is calculated with the perturbation theory in a magnetic field B, where we take $B = B_0$ for (a), and $B = 0.5B_0$ in (b) and (c) for illustrative purpose, and $B_0 = (ch/e)/L_x^2$.

Applying the above conditions to Eq. (6), we obtain

$$\begin{pmatrix} 1 & 1 & 1 & 1 \\ e^{i\theta} & -e^{-i\theta} & -e^{-i\theta} & e^{i\theta} \\ e^{i\lambda} & e^{-i\lambda} & \alpha e^{i\lambda} & \alpha e^{-i\lambda} \\ e^{i(\lambda+\theta)} & -e^{-i(\lambda+\theta)} & -\alpha e^{i(\lambda+\theta)} & \alpha e^{-i(\lambda+\theta)} \end{pmatrix} \begin{pmatrix} A \\ B \\ C \\ D \end{pmatrix} = \begin{pmatrix} 0 \\ 0 \\ 0 \\ 0 \end{pmatrix}, \tag{14}$$

where $\alpha = \omega^{-2N}$ and $\lambda = k_x L_x$. The determinant of matrix in Eq. (14) should vanish to have a nonzero solution. This condition is reduced to

$$k_x = k_n \equiv \frac{\pi}{L_x}\left(n - \frac{\nu}{3}\right), \quad n = 0, \pm 1, \pm 2, \ldots, \tag{15}$$

ν is an integer $(0, \pm 1)$ defined by

$$2N = 3m + \nu, \tag{16}$$

with integer m. The eigenstate and energy are obtained as

$$\boldsymbol{F}_{snk_y}(\boldsymbol{r}) = \frac{e^{ik_y y}}{2\sqrt{L_x L_y}} \begin{pmatrix} e^{ik_n x} \\ s e^{i(k_n x + \theta)} \\ -e^{-ik_n x} \\ s e^{-i(k_n x - \theta)} \end{pmatrix},$$

$$\varepsilon_{snk_y} = s\hbar v \sqrt{k_n^2 + k_y^2}. \tag{17}$$

When $\nu = 0$, the energy bands of $n = 0$ and $s = \pm$ stick together and thus the system is metallic, while otherwise a gap opens at zero energy and the system becomes a semiconductor. Energy bands for metallic armchair ribbon $(\nu = 0)$ and semiconducting armchair ribbon $(\nu = \pm 1)$ are shown in Figs. 3(b) and 3(c), respectively. In (c), the labeling n is for the case of $\nu = +1$, while n becomes $-n$ in $\nu = -1$.

D. Orbital susceptibility

To calculate the orbital diamagnetism, we consider a graphene ribbon under a uniform magnetic field B perpendicular to the graphene plane. We take the Landau gauge and set the vector potential as

$$\boldsymbol{A}(\boldsymbol{r}) = \left[0, B\left(x - \frac{L_x}{2}\right)\right]. \tag{18}$$

The Hamiltonian in presence of the magnetic field is obtained by replacing $\hat{\boldsymbol{k}}$ by $\hat{\boldsymbol{k}} + e\boldsymbol{A}/(\hbar c)$, as

$$\mathcal{H} = \mathcal{H}_0 + \delta\mathcal{H}, \quad \delta\mathcal{H} = \frac{e}{c}\hat{v}_y A_y, \tag{19}$$

where c is the light velocity, and

$$\hat{v}_y = \frac{1}{\hbar}\frac{\partial \mathcal{H}}{\partial \hat{k}_y} = v \begin{pmatrix} 0 & -i & 0 & 0 \\ i & 0 & 0 & 0 \\ 0 & 0 & 0 & i \\ 0 & 0 & -i & 0 \end{pmatrix}. \tag{20}$$

The operator of the electric current density is given by

$$\hat{j}_y(\boldsymbol{r}) = -\frac{e}{2}\{\hat{v}_y \delta(\boldsymbol{r} - \boldsymbol{r}') + \delta(\boldsymbol{r} - \boldsymbol{r}')\hat{v}_y\}. \tag{21}$$

In the first-order perturbation in $\delta\mathcal{H}$, the expectation value of the current density is written as

$$j_y(\boldsymbol{r}) = \sum_\alpha f(\varepsilon_\alpha) \sum_{\beta(\neq\alpha)} \frac{2\mathrm{Re}[(\delta\mathcal{H})_{\alpha\beta}[\hat{j}_y(\boldsymbol{r})]_{\beta\alpha}]}{\varepsilon_\alpha - \varepsilon_\beta}, \tag{22}$$

where α and β represent the unperturbed eigenstates of graphene ribbon, and $f(\varepsilon) = 1/[1 + e^{\beta(\varepsilon-\mu)}]$ is the Fermi distribution function with the chemical potential μ.

In a zigzag ribbon, the current density always vanishes at the edges $x = 0$ and L_x, while it is not generally the case in armchair ribbons. This is obvious from the matrix element of $\hat{j}_y$ between two eigenstates $\boldsymbol{F}$ and $\boldsymbol{F}'$,

$$\langle \boldsymbol{F}' | \hat{j}_y(\boldsymbol{r}) | \boldsymbol{F} \rangle = iev\left[F_{\mathrm{A}}'^{\mathrm{K}}(\boldsymbol{r})^* F_{\mathrm{B}}^{\mathrm{K}}(\boldsymbol{r}) - F_{\mathrm{B}}'^{\mathrm{K}}(\boldsymbol{r})^* F_{\mathrm{A}}^{\mathrm{K}}(\boldsymbol{r})\right]. \tag{23}$$

In the wave function of the zigzag ribbon, Eqs. (10) and (12), the component $F_{\mathrm{A}}^{\mathrm{K}}$ is zero at $x = 0$, and $F_{\mathrm{B}}^{\mathrm{K}}$ is at L_x, so that Eq. (23) vanishes at both edges.

The current density on the xy plane is related to the local magnetic moment $m(\boldsymbol{r})$ in the z direction by

$$j_x = c\frac{\partial m}{\partial y}, \quad j_y = -c\frac{\partial m}{\partial x}. \tag{24}$$

In the present case, $m(\boldsymbol{r})$ depends only on x so that the total magnetization per area is

$$\begin{aligned} M &= \frac{1}{L_x L_y}\int_0^{L_x}\int_0^{L_y} m(x)\,dx\,dy \\ &= \frac{1}{cL_x}\int_0^{L_x}\left(x - \frac{L_x}{2}\right) j_y(x)\,dx. \end{aligned} \tag{25}$$

The magnetic susceptibility is written as

$$\chi = \lim_{B\to 0}\frac{M}{B} = \frac{2}{cL_x L_y}\sum_\alpha f(\varepsilon_\alpha)\sum_{\beta(\neq\alpha)}\frac{|(\delta\mathcal{H}/B)_{\alpha\beta}|^2}{\varepsilon_\beta - \varepsilon_\alpha}. \tag{26}$$

We calculate Eqs. (22) and (26) numerically. As we have infinite energy bands below zero, we introduce a cutoff function $g(\varepsilon_\alpha)$ which smoothly vanishes $|\varepsilon_\alpha| > \varepsilon_c$. In the following, we take $\varepsilon_c = 50\varepsilon_0$ where

$$\varepsilon_0 = \frac{2\pi\hbar v}{L_x} \tag{27}$$

is the typical energy scale for the subband structure. The result is actually converging in the limit of large ε_c.

The susceptibility of the infinite bulk graphene at zero temperature is given by[1,13,19]

$$\chi_{\mathrm{gr}}(\varepsilon_F) = -g_v g_s \frac{e^2 v^2}{6\pi c^2}\delta(\varepsilon_F), \tag{28}$$

where $g_v = g_s = 2$ are the valley and spin degeneracies, respectively. At finite temperature, it becomes

$$\begin{aligned} \chi_{\mathrm{gr}}(\mu; T) &= \int_{-\infty}^{\infty} d\varepsilon \left(-\frac{\partial f(\varepsilon)}{\partial \varepsilon}\right)\chi_{\mathrm{gr}}(\varepsilon) \\ &= -g_v g_s \frac{e^2 v^2}{24\pi c^2}\frac{1}{k_B T \cosh^2[\mu/(2k_B T)]}. \end{aligned} \tag{29}$$

In the graphene ribbon, the characteristic unit of the susceptibility can be chosen as

$$\chi_0 = g_v g_s \frac{e^2 v^2}{6\pi c^2} \frac{1}{\varepsilon_0}. \tag{30}$$

III. NUMERICAL RESULTS

A. Magnetic susceptibility

The lower panels of Fig. 3 show the orbital susceptibility $\chi(\varepsilon_F)$ of (a) zigzag, (b) metallic armchair ($\nu = 0$), and (c) semiconducting armchair ($\nu = \pm 1$) ribbons at zero temperature, where the upward direction represents the negative (i.e., diamagnetic) susceptibility. The figures are to be compared with the band structures in the upper panels. In every case, the magnitude of χ becomes the maximum at $\varepsilon_F = 0$, and oscillates as a function of ε_F in accordance with the subband structure. In the positive energy region, for example, the curve sharply rises when a subband starts to be occupied by electrons, while it tends to decrease otherwise. In large $|\varepsilon_F|$, the amplitude of the oscillation slowly attenuates approximately in proportion to $1/\sqrt{|\varepsilon_F|}$.

The oscillating feature can be understood in terms of the band energy shift in an infinitesimal magnetic field. In the upper panels of Fig. 3, we plot as broken curves the energy band in some small B calculated by the second-order perturbation. Here the amplitude B is set to some finite value for illustrative purpose. Generally the system is diamagnetic when the total-energy shift caused by B is positive, and paramagnetic when negative. In the metallic armchair ribbon (b), for example, we see that a pair of the first subbands ($n = 0, s = \pm$) shift toward zero energy, due to the level repulsions from excited subbands nearby. All other bands ($|n| \geqslant 1$) move in the opposite direction away from zero energy, while the absolute shifts are much smaller than that of $n = 0$.

When ε_F is zero, the energy gain of the first valence band ($s = -, n = 0$) exceeds the energy loss of all other valence bands ($s = -, |n| \geqslant 1$), resulting in the total diamagnetism. When ε_F is shifted to the positive side, the diamagnetism decreases because the first conduction band ($s = +, n = 0$) has a negative shift and gives paramagnetism. When the second conduction band ($s = +, |n| = 1$) starts to be filled, the susceptibility suddenly jumps to the diamagnetic direction, because the shift is positive there and also the density of states diverges at the band bottom. The oscillation of other types, (a) and (c), can be explained in a similar manner.

In Fig. 4, the susceptibility at several different temperatures is plotted as a function of the chemical potential μ. We here choose the metallic armchair ribbon ($\nu = 0$) while the qualitative property is the same in other cases. We see that the oscillation rapidly disappears once $k_B T$ becomes of the order of ε_0, i.e., the thermal broadening energy is as large as the subband interval energy, and we are left with only a single diamagnetic peak at $\varepsilon_F = 0$. When $k_B T \gtrsim \varepsilon_0$, the curve becomes almost identical with the bulk susceptibility, Eq. (29), or the thermally broadened δ function. When we fix the temperature and increase the ribbon width instead, we would see that the oscillatory curve of $\chi(\mu)$ is shrinking in the horizontal direction as the energy scale ε_0 decreases, and, once ε_0 becomes as small as $k_B T$, the oscillation vanishes and the curve goes to the bulk limit. Similar behavior is observed in all the types of ribbons considered here, and the finite-size effect always disappears when $k_B T \gtrsim \varepsilon_0$ regardless of the edge configuration.

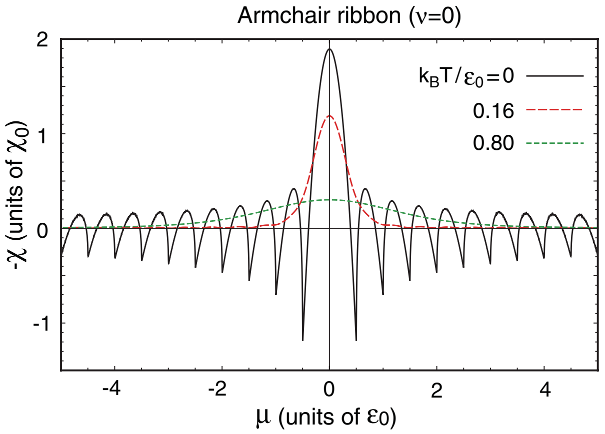

FIG. 4. (Color online) Magnetic susceptibility against chemical potential μ for metallic armchair ribbon ($\nu = 0$) at several different temperatures.

B. Diamagnetic current density

Figure 5 shows the diamagnetic current density $j_y(x)$ in different types of graphene ribbons at $\varepsilon_F = 0$ and $T = 0$, calculated in the first-order perturbation of B. The unit of current density is taken as $c\chi_0 B/L_x$. The current flows in opposite directions in the left-hand side and right-hand side of the ribbon, to make a magnetization perpendicular to the layer. Reflecting the absence of the characteristic length scale, the current distribution is not localized to the edge but spread in the entire width in a form of slowly varying monotonic function.

In zigzag ribbons, the current density actually becomes absolute zero at $x = 0$ and L_x, in accordance with the constraint argued in the previous section. The current sharply drops to zero at the edges, and some oscillatory feature remains around the edge due to a finite cutoff energy. When we increase the energy cutoff (not shown), the curve appears to slowly

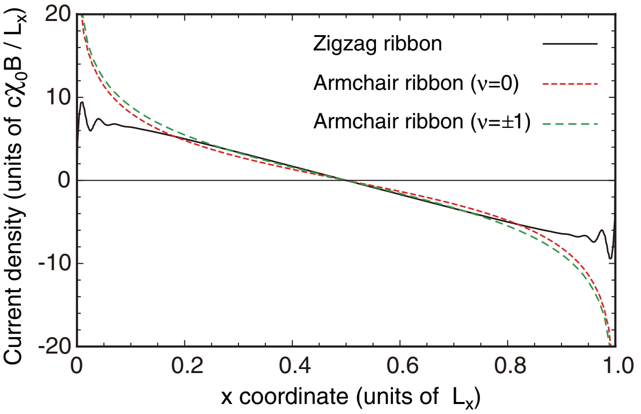

FIG. 5. (Color online) Diamagnetic current density $j_y(x)$ of different types of graphene ribbons with $\varepsilon_F = 0$ at $T = 0$.

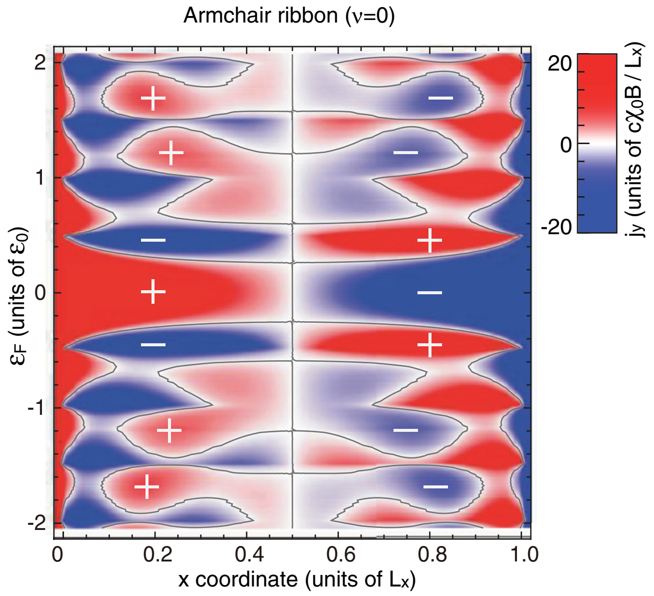

FIG. 6. (Color online) Two-dimensional density plot $j_y(x;\varepsilon_F)$ of the diamagnetic current density of metallic armchair ribbon ($\nu = 0$), as a function of position x (horizontal axis) and Fermi energy (vertical).

approach a fixed curve having a discontinuous jump at the edges. In the armchair ribbons, j_y is not necessarily zero but logarithmically diverges at the both edges. The numerical calculation converges much more rapidly there, since there is no discontinuity as in the zigzag case.

Figure 6 is the two-dimensional density plot $j_y(x;\varepsilon_F)$ of the diamagnetic current density of metallic armchair ribbon, as a function of position x (horizontal axis) and Fermi energy (vertical). In increasing ε_F, the current distribution begins to oscillate as a function of x, with a characteristic wave number of the order of $k_F = \varepsilon_F/(\hbar v)$.

The temperature dependence of the current density at $\varepsilon_F = 0$ is shown in Fig. 7 for the same metallic armchair ribbon. When k_BT becomes as large as ε_0, the current distribution is localized at the boundary forming the counter edge currents. This is the same temperature range where the oscillation of χ disappears and the bulk limit is achieved. The depth of the current distribution is characterized by

$$\lambda_{\text{edge}}(T) = \frac{\hbar v}{2\pi k_B T}, \tag{31}$$

which shrinks in increasing temperature. With the band velocity of graphene, $v \approx 10^6$ m/s, it is estimated as $\lambda_{\text{edge}} \approx [1/T(K)]\ \mu$m.

This behavior is intuitively explained using the plot of $j_y(x;\varepsilon_F)$ in Fig. 6. The current density at a finite T is obtained by integrating $j_y(x;\varepsilon_F)$ in ε_F with the thermal averaging factor $-\partial f/\partial\varepsilon$. The current of the middle part of the ribbon vanishes in averaging the oscillating function in ε_F, while the cancellation is not complete only near the edges, since j_y is always positive and negative in the left and right ends, respectively. The similar temperature dependence of the current distribution is found in other types of ribbons considered here. This suggests that, in any finite pieces of graphene with length scale L, the finite-size effect disappears when $k_BT \gtrsim \varepsilon_0$, and then the diamagnetic current circulates only near the edge with a depth λ_{edge}.

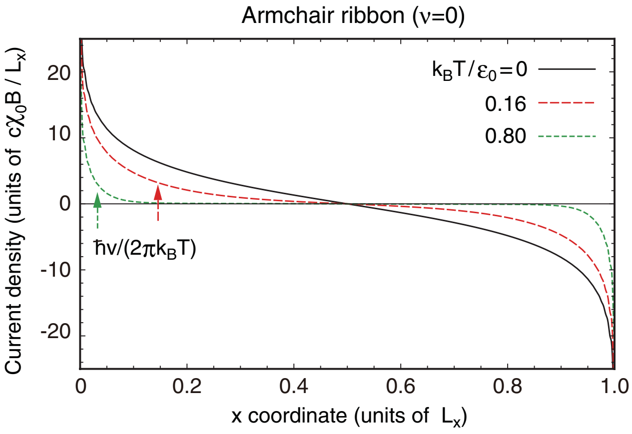

FIG. 7. (Color online) Diamagnetic current density $j_y(x)$ of metallic armchair ribbon ($\nu = 0$) with $\varepsilon_F = 0$, at several different temperatures. The vertical arrows indicate the characteristic length scale $\hbar v/(2\pi k_BT)$ measured from $x = 0$.

C. Relation to spin paramagnetism

We neglect the effect of the electron spin throughout the present analysis. In a zigzag ribbon, particularly, the large density of states contributed by the zero-energy flat band is expected to give a significant magnitude of Pauli paramagnetism and reduce the orbital diamagnetism.[31]

The ratio between two effects can be quantitatively estimated as follows. The susceptibility of Pauli paramagnetism is given by

$$\chi_{\text{para}} = \left(\frac{g}{2}\right)\mu_B^2 D(\varepsilon), \tag{32}$$

where $g \sim 2$ is the g factor for a graphene electron, $\mu_B = e\hbar/(2mc)$ is the Bohr magneton with m being the free-electron mass, and $D(\varepsilon)$ is the density of states per area given by the zero-energy flat band. Since the number of edge states accommodated in a ribbon of the length L is $\sim L/a$ per spin and per valley,[31] we have

$$D(\varepsilon) \sim \frac{g_v g_s}{L^2}\frac{L}{a}\delta(\varepsilon), \tag{33}$$

which gives a δ function singularity in χ_{para}.

By comparing χ_{para} with the bulk orbital diamagnetism χ_{dia}, Eq. (28), we obtain

$$\left|\frac{\chi_{\text{para}}}{\chi_{\text{dia}}}\right| = \frac{3\pi}{2}\frac{\hbar^2}{m^2v^2aL} \sim 1.0 \times \frac{a}{L}, \tag{34}$$

which is negligible in a wide strip with $L \gg a$. In a low temperature such that $k_BT \lesssim \varepsilon_0$, however, χ_{dia} cannot be regarded as thermally broadened δ function due to the effect of the subband formation, and then χ_{para} overcomes χ_{dia} only at $\varepsilon_F = 0$.

IV. CARBON NANOTUBES

The carbon nanotube is a quasi-one-dimensional system similar to graphene ribbon, but different in that there are no edges.[52,53] Experimentally, graphene nanoribbons with smooth edges can be obtained by unzipping the carbon nanotubes, i.e., lengthwise cutting of carbon nanotube sidewalls.[40,41] Then we may ask which of the ribbon and the original nanotube has greater diamagnetism, and how the susceptibility oscillation in ε_F changes in unzipping. The orbital susceptibility of carbon nanotube was theoretically studied for small Fermi energies in the effective-mass approximation.[22,23] Here we compute full Fermi energy dependence in parallel fashion to the analysis for ribbons.

A carbon nanotube is characterized by a chiral vector,

$$\boldsymbol{L} = n_a \boldsymbol{a} + n_b \boldsymbol{b}, \tag{35}$$

where the atom at $\boldsymbol{L}$ on a graphene sheet is rolled up onto the origin in constructing a tube. The boundary condition is given by $\psi_{\mathrm{A}}(\boldsymbol{R}_{\mathrm{A}}) = \psi_{\mathrm{A}}(\boldsymbol{R}_{\mathrm{A}} + \boldsymbol{L})$ and $\psi_{\mathrm{B}}(\boldsymbol{R}_{\mathrm{B}}) = \psi_{\mathrm{B}}(\boldsymbol{R}_{\mathrm{B}} + \boldsymbol{L})$. For the effective-mass wave function, it is written as[50]

$$\begin{aligned} \boldsymbol{F}^{\mathrm{K}}(\boldsymbol{r} + \boldsymbol{L}) &= \exp\left(-\frac{2\pi i}{3}\nu\right) \boldsymbol{F}^{\mathrm{K}}(\boldsymbol{r}), \\ \boldsymbol{F}^{\mathrm{K}'}(\boldsymbol{r} + \boldsymbol{L}) &= \exp\left(+\frac{2\pi i}{3}\nu\right) \boldsymbol{F}^{\mathrm{K}'}(\boldsymbol{r}). \end{aligned} \tag{36}$$

Here $\boldsymbol{F}^{\mathrm{K}} = (F_{\mathrm{A}}^{\mathrm{K}}, F_{\mathrm{B}}^{\mathrm{K}})$, etc., and ν is an integer $(0,\pm 1)$ defined by

$$n_a + n_b = 3m + \nu, \tag{37}$$

with integer m.

For K point, the eigenstates are immediately obtained as

$$\begin{aligned} \boldsymbol{F}^{\mathrm{K}}_{snk_y}(\boldsymbol{r}) &= \frac{e^{ik_y y}}{\sqrt{2L_x L_y}} \begin{pmatrix} e^{ik_n x} \\ s e^{i(k_n x + \theta)} \\ 0 \\ 0 \end{pmatrix}, \\ \varepsilon_{snk_y} &= s\hbar v \sqrt{k_y^2 + k_n^2}, \end{aligned} \tag{38}$$

where

$$k_n \equiv \frac{2\pi}{L_x}\left(n - \frac{\nu}{3}\right), \quad n = 0, \pm 1, \pm 2, \ldots, \tag{39}$$

and $L_x = |\boldsymbol{L}|$ and L_y is length of the carbon nanotube. The system is metallic when $\nu = 0$, and semiconducting when $\nu = \pm 1$. The band structure looks similar to armchair graphene ribbons, but the unit of momentum quantization doubled compared to Eq. (15), leading to wider energy spacing between subbands. The energy band for K′ is obtained by replacing k_y by $-k_y$ and also ν by $-\nu$.

When a uniform magnetic field B is applied perpendicularly to the nanotube axis, the vector potential can be taken as

$$\boldsymbol{A}(\boldsymbol{r}) = \left(0, \frac{BL_x}{2\pi} \sin\frac{2\pi x}{L_x}\right). \tag{40}$$

We should note that the expression differs from that for ribbon, Eq. (18), because the magnetic field perpendicular to the tube surface is not a constant, but a sinusoidal function in x. Except for that, the magnetic susceptibility $\chi_{\mathrm{tube}}(\varepsilon_F)$ is calculated in the same formula, Eq. (26).

The susceptibility of the carbon nanotube is naturally related to that of graphene against a spatial varying magnetic field $B(q)\sin qx$ with $q = 2\pi/L_x \equiv q_0$. When we define the q-dependent susceptibility of graphene as $\chi_{\mathrm{gr}}(q) \equiv m(q)/B(q)$,[16] we obtain a relation

$$\langle \chi_{\mathrm{tube}}(\varepsilon_F) \rangle_\varphi = \tfrac{1}{2}\chi_{\mathrm{gr}}(q_0; \varepsilon_F). \tag{41}$$

Here $\langle\,\rangle_\varphi$ represents an average over a phase factor φ which twists the boundary condition of carbon nanotube as $\psi(\boldsymbol{r} + \boldsymbol{L}) = \exp(2\pi i\varphi)\psi(\boldsymbol{r})$. Physically, the phase factor corresponds to threading a magnetic flux of $(ch/e)\varphi$ into the nanotube cross section.[22,50] It changes momentum quantization of Eq. (39) to $k_n = (2\pi/L_x)(n + \varphi - \nu/3)$, and the flux averaging over φ smears the difference in ν. The factor 1/2 in Eq. (41) enters because the average of the squared magnetic field on the nanotube surface is $B(q_0)^2/2$.

At the zero temperature, $\chi_{\mathrm{gr}}(q;\varepsilon_F)$ is explicitly evaluated as[16]

$$\begin{aligned} \chi_{\mathrm{gr}}(q;\varepsilon_F) = &-\frac{g_v g_s e^2 v}{16\hbar c^2}\frac{1}{q}\theta(q - 2k_F) \\ &\times \left[1 + \frac{2}{\pi}\frac{2k_F}{q}\sqrt{1 - \left(\frac{2k_F}{q}\right)^2} - \frac{2}{\pi}\sin^{-1}\frac{2k_F}{q}\right], \end{aligned} \tag{42}$$

where $k_F = |\varepsilon_F|/(\hbar v)$ is the Fermi wave number and $\theta(x)$ is defined by $\theta(x) = 1\ (x > 0)$ and $0\ (x < 0)$. Using Eqs. (41) and (42), the flux-averaged susceptibility integrate is shown to be

$$\left\langle \int_{-\infty}^{\infty} \chi_{\mathrm{tube}}(\varepsilon_F)\, d\varepsilon_F \right\rangle_\varphi = \frac{1}{2}\left(-g_v g_s \frac{e^2 v^2}{6\pi c^2}\right), \tag{43}$$

which is exactly half of graphene's, suggesting that the susceptibility is effectively smaller in nanotube than in ribbon. This is simply because the B-field component penetrating the lattice plane is smaller in the nanotube due to its cylindrical shape.

The susceptibility before taking flux average can be calculated in numerics. Figure 8(a) shows $\chi_{\mathrm{tube}}(\varepsilon_F)$ for the metallic $(\nu = 0)$ and the semiconducting $(\nu = \pm 1)$ nanotubes, together with the flux average. It has an oscillatory behavior similar to the graphene ribbon's, while χ in $|\varepsilon_F| > \hbar v q/2$ completely vanishes after flux average.[16] In increasing temperature (not shown), the oscillation immediately disappears, leaving a single peak regardless of ν, similar to the graphene ribbon.

Figure 8(b) compares the susceptibility of a carbon nanotube and that of corresponding graphene ribbon unzipped from the same nanotube. Here we chose a zigzag ribbon as an example, when the corresponding nanotube becomes an armchair nanotube which is always metallic $(\nu = 0)$.[50] The oscillation period of the nanotube is approximately twice as large as that of the ribbon, reflecting the wider subband spacing. Overall magnitude of χ is smaller in nanotube roughly by factor 2. The integrate of susceptibility in ε_F differs in factor 2 in numerical accuracy, in accordance with the above arguments.

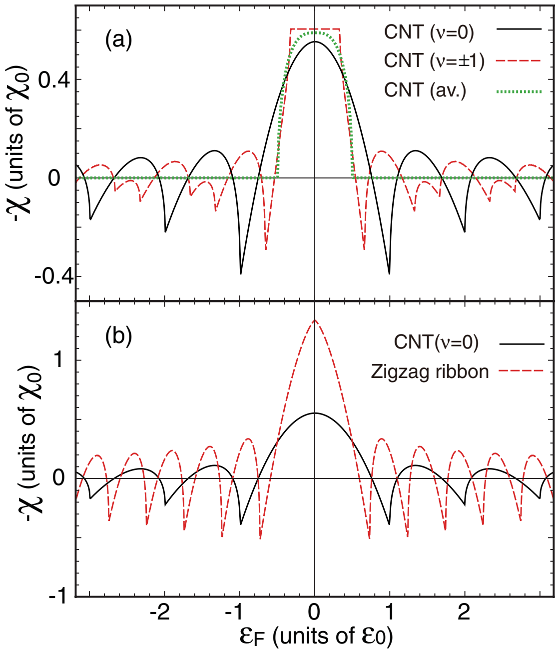

FIG. 8. (Color online) (a) Magnetic susceptibility of carbon nanotubes. Solid (black), dashed (red), and dotted (green) curves are for metallic ($\nu = 0$), semiconducting ($\nu = \pm 1$), and the flux average, respectively. (b) Magnetic susceptibility of the carbon nanotube of $\nu = 0$ (solid black) and the zigzag ribbon unzipped from the same nanotube (dashed red).

V. RANDOMLY STACKED MULTILAYER GRAPHENE

The diamagnetism can be made even greater by stacking graphenes in three dimensions. The recent experimental technique realizes a novel kind of graphene multilayer in which successive layers are stacked with random rotating angles.[43–45] There it is known that the interlayer coupling is significantly weakened and the Dirac cone is kept almost intact near zero energy as long as the rotating angle is not too small.[46–49] The orbital susceptibility of such a system is expected to be much stronger than graphite in which the δ function peak of $\chi(\varepsilon_F)$ is much broadened and shortened by the regular interlayer coupling.[18,25]

Here we consider the orbital diamagnetism of a finite-sized piece of random-stacked graphene multilayers. In calculations, we self-consistently include the effect of the counter-magnetic field induced by the diamagnetic current itself. This is essential because, as we will show in the following, the counter-magnetic field of this system can be of the same order of the external magnetic field, and even nearly perfect screening is possible in low temperatures.

For simplicity, we completely neglect the interlayer coupling and regard the system as a set of independent single layer graphenes. We also assume that each layer has the identical shape with a characteristic length scale L, and that the system is large enough that the thermal broadening energy $k_B T$ is much larger than $2\pi\hbar v/L$. According to the previous discussions, we then expect that the susceptibility of each layer is given by the bulk limit χ_{gr} in Eq. (29), and also the depth of the edge current λ_{edge} of Eq. (31) can be neglected with respect to the system size L.

Let us consider a situation where a external field B_{ext} is applied perpendicularly to graphene plane of the random stacked multilayer. The total magnetic field B penetrating the system is

$$B = B_{\text{ext}} + \Delta B, \tag{44}$$

where ΔB is the counter field caused by graphene electrons. The total field B induces the magnetism in each layer, $M = \chi_{\text{gr}} B S$, with S being the area of the layer. This is related to the diamagnetic edge current I of each single layer by

$$I = \frac{cM}{S} = c\chi_{\text{gr}} B. \tag{45}$$

Since the ring current I exists every interlayer distance d, it induces a counter-magnetic field inside the system as

$$\Delta B = \frac{4\pi}{c}\frac{I}{d}. \tag{46}$$

Solving the set of equations, we find that the dimensionless volume susceptibility becomes

$$\chi_{\text{3D}} \equiv \frac{\Delta B}{B_{\text{ext}}} = \frac{-1}{1 - d/(4\pi\chi_{\text{gr}})}. \tag{47}$$

At the charge neutral point $\mu = 0$, in particular, we have

$$\chi_{\text{3D}}(\mu = 0) = \frac{-1}{1 + k_B T/\Delta}, \tag{48}$$

where Δ is a characteristic energy scale defined by

$$\Delta = \frac{g_v g_s}{6}\left(\frac{v}{c}\right)^2 \frac{e^2}{d} \approx 0.03 \ \text{meV}, \tag{49}$$

and d is assumed to be the interlayer spacing of graphite, 0.334 nm.

In decreasing the temperature, χ_{3D} monotonically increases in the negative direction, and approaches -1, where the perfect magnetic-field screening is achieved. This reflects the property of the single-layer susceptibility, Eq. (29), of which peak value at the Dirac point diverges in $T \to 0$. In contrast, χ_{3D} of the graphite is of the order of 10^{-4} and is not much enhanced in low temperatures,[54–57] because $\chi(\varepsilon_F)$ is already broadened by the interlayer coupling energy about 4000 K.[18,25] A three-dimensional bulk material composed of random-stacked graphenes, if realized, would be a stronger diamagnetic material than any other known substance except for the superconductors. Including the effect of the residual interlayer coupling between misoriented layers may set the upper limit to χ_{3D}, while we leave the detailed analysis for a future problem.

VI. CONCLUSION

We have studied the orbital diamagnetism of graphene ribbons using the effective-mass approximation, to figure out its dependence on temperature and Fermi energy, and also the finite-size effect on the δ function singularity in the bulk limit. In increasing temperature, an oscillatory behavior in the orbital susceptibility $\chi(\varepsilon_F)$ is eventually smeared out, approaching the bulk limit, i.e., a thermally broadened δ function centered at $\varepsilon_F = 0$. The electric current responsible for the diamagnetism spreads entirely in the sample at $T = 0$ reflecting the absence of the characteristic wavelength, while as T is increased, the current density tends to localize near the edge with a depth $\sim\hbar v/(2\pi k_B T)$.

We also see a carbon nanotube, another form of quasi-one-dimensional carbon, exhibits a similar oscillation in $\chi(\varepsilon_F)$, but the overall magnitude is reduced by a factor 2 compared to the corresponding ribbon having the same width. The result is applied to estimate the three-dimensional bulk susceptibility of random-stacked multilayer graphene. There we showed that the external magnetic field is significantly screened inside the sample.

ACKNOWLEDGMENTS

This project has been funded by JST-EPSRC Japan-UK Cooperative Programme Grant No. EP/H025804/1.

---

[1] J. W. McClure, Phys. Rev. **104**, 666 (1956).

[2] J. W. McClure, Phys. Rev. **119**, 606 (1960).

[3] M. P. Sharma, L. G. Johnson, and J. W. McClure, Phys. Rev. B **9**, 2467 (1974).

[4] K. S. Novoselov, A. K. Geim, S. V. Morozov, D. Jiang, Y. Zhang, S. V. Dubonos, I. V. Grigorieva, and A. A. Firsov, Science **306**, 666 (2004).

[5] K. S. Novoselov, A. K. Geim, S. V. Morozov, D. Jiang, M. I. Katsnelson, I. V. Grigorieva, S. V. Dubonos, and A. A. Firsov, Nature (London) **438**, 197 (2005).

[6] Y. Zhang, Y.-W. Tan, H. L. Stormer, and P. Kim, Nature (London) **438**, 201 (2005).

[7] J. C. Slonczewski and P. R. Weiss, Phys. Rev. **109**, 272 (1958).

[8] D. P. DiVincenzo and E. J. Mele, Phys. Rev. B **29**, 1685 (1984).

[9] G. W. Semenoff, Phys. Rev. Lett. **53**, 2449 (1984).

[10] S. G. Sharapov, V. P. Gusynin, and H. Beck, Phys. Rev. B **69**, 075104 (2004).

[11] H. Fukuyama, J. Phys. Soc. Jpn. **76**, 043711 (2007).

[12] M. Nakamura, Phys. Rev. B **76**, 113301 (2007).

[13] M. Koshino and T. Ando, Phys. Rev. B **75**, 235333 (2007).

[14] A. Ghosal, P. Goswami, and S. Chakravarty, Phys. Rev. B **75**, 115123 (2007).

[15] T. Ando, Physica E **40**, 213 (2007).

[16] M. Koshino, Y. Arimura, and T. Ando, Phys. Rev. Lett. **102**, 177203 (2009).

[17] M. Koshino and T. Ando, Phys. Rev. B **81**, 195431 (2010).

[18] S. A. Safran, Phys. Rev. B **30**, 421 (1984).

[19] S. A. Safran and F. J. DiSalvo, Phys. Rev. B **20**, 4889 (1979).

[20] J. Blinowski and C. Rigaux, J. Phys. (Paris) **45**, 545 (1984).

[21] R. Saito and H. Kamimura, Phys. Rev. B **33**, 7218 (1986).

[22] H. Ajiki and T. Ando, J. Phys. Soc. Jpn. **62**, 2470 (1993); **63**, 4267(E) (1994).

[23] H. Ajiki and T. Ando, J. Phys. Soc. Jpn. **64**, 4382 (1995).

[24] M. Yamamoto, M. Koshino, and T. Ando, J. Phys. Soc. Jpn. **77**, 084705 (2008).

[25] M. Koshino and T. Ando, Phys. Rev. B **76**, 085425 (2007).

[26] M. Nakamura and L. Hirasawa, Phys. Rev. B **77**, 045429 (2008).

[27] A. H. Castro Neto, F. Guinea, N. M. Peres, K. S. Novoselov, and A. K. Geim, Rev. Mod. Phys. **81**, 109 (2009).

[28] A. Kobayashi, Y. Suzumura, and H. Fukuyama, J. Phys. Soc. Jpn. **77**, 064718 (2008). Hall effect and orbital diamagnetism in zerogap state of molecular conductor α-(BEDT-TTF)$_2$I$_3$.

[29] M. Fujita, K. Wakabayashi, K. Nakada, and K. Kusakabe, J. Phys. Soc. Jpn. **65**, 1920 (1996).

[30] K. Nakada, M. Fujita, G. Dresselhaus, and M. S. Dresselhaus, Phys. Rev. B **54**, 17954 (1996).

[31] K. Wakabayashi, M. Fujita, H. Ajiki, and M. Sigrist, Phys. Rev. B **59**, 8271 (1999).

[32] M. Ezawa, Phys. Rev. B **73**, 045432 (2006).

[33] L. Brey and H. Fertig, Phys. Rev. B **73**, 195408 (2006).

[34] L. Brey and H. Fertig, Phys. Rev. B **73**, 235411 (2006).

[35] Y-W. Son, M. L. Cohen, and S. G. Louie, Phys. Rev. Lett. **97**, 216803 (2006).

[36] Y-W. Son, M. L. Cohen, and S. G. Louie, Nature (London) **444**, 347 (2006).

[37] M. Y. Han, B. Özyilmaz, Y. Zhang, and P. Kim, Phys. Rev. Lett. **98**, 206805 (2007).

[38] Z. Chen, Y.-M. Lin, M. J. Rooks, and P. Avouris, Physica E **40**, 228 (2007).

[39] X. Li, X. Wang, L. Zhang, S. Lee, and H. Dai, Science **319**, 1229 (2008).

[40] D. V. Kosynkin, A. L. Higginbotham, A. Sinitskii, J. R. Lomeda, A. Dimiev, B. K. Price, and J. M. Tour, Nature (London) **458**, 872 (2009).

[41] L. Y. Jiao, L. Zhang, X. R. Wang, G. Diankov, and H. J. Dai, Nature (London) **458**, 877 (2009).

[42] J. Liu, Z. Ma, A. R. Wright, and Chao Zhang, J. Appl. Phys. **103**, 103711 (2008).

[43] C. Berger, Z. Song, X. Li, X. Wu, N. Brown, C. Naud, D. Mayou, T. Li, J. Hass, A. N. Marchenkov, E. H. Conrad, P. N. First, and W. A. de Heer, Science **312**, 1191 (2006).

[44] J. Hass, R. Feng, J. E. Millan-Otoya, X. Li, M. Sprinkle, P. N. First, W. A. de Heer, E. H. Conrad, and C. Berger, Phys. Rev. B **75**, 214109 (2007).

[45] G. Li, A. Luican, and E. Y. Andrei, Phys. Rev. Lett. **102**, 176804 (2009).

[46] J. M. B. Lopes dos Santos, N. M. R. Peres, and A. H. Castro Neto, Phys. Rev. Lett. **99**, 256802 (2007).

[47] S. Latil, V. Meunier, and L. Henrard, Phys. Rev. B **76**, 201402(R) (2007).

[48] S. Shallcross, S. Sharma, and O. A. Pankratov, Phys. Rev. Lett. **101**, 056803 (2008).

[49] E. J. Mele, Phys. Rev. B **81**, 161405 (2010).

[50] T. Ando, J. Phys. Soc. Jpn. **74**, 777 (2005).

[51] N. H. Shon and T. Ando, J. Phys. Soc. Jpn. **67**, 2421 (1998).

[52] S. Iijima, Nature (London) **354**, 56 (1991).

[53] S. Iijima, T. Ichihashi, and Y. Ando, Nature (London) **356**, 776 (1992).

[54] V. P. Gusynin and S. G. Sharapov, Phys. Rev. Lett. **95**, 146801 (2005).

[55] N. M. R. Peres, F. Guinea, and A. H. Castro Neto, Phys. Rev. B **73**, 125411 (2006).

[56] P. Marconcini and M. Macucci, Riv. Nuovo Cimento **34**, 489 (2011).

[57] K. S. Krishnan and N. Ganguli, Nature (London) **139**, 155 (1937).